# A Test of Energetic Particle Precipitation Models Using Simultaneous Incoherent Scatter Radar and Van Allen Probes Observations

Ennio R. Sanchez[1], Qianli Ma[2,5], Wei Xu[3], Robert A. Marshall[3], Jacob Bortnik[2], Pablo Reyes[1], Roger Varney[1], Stephen Kaeppler[4]

[1]Center for Geospace Studies, SRI International
[2]Department of Atmospheric and Oceanic Sciences, University of California Los Angeles
[3]Department of Aerospace Engineering Sciences, University of Colorado Boulder
[4]Department of Physics and Astronomy, Clemson University
[5]Center for Space Physics, Boston University

**Key points**

- Comparison between observed and modeled density for electron precipitation due to wave-particle interactions in the magnetosphere
- Comparison verifies the validity of D-region electron density predicted by pitch-angle diffusion models of wave-particle interaction
- Observed electron profiles are obtained with an incoherent scatter radar mode especially designed to optimize measurements in the D-region

**Abstract**

Quantification of energetic electron precipitation caused by wave-particle interactions is fundamentally important to understand the cycle of particle energization and loss of the radiation belts. One important way to determine how well the wave-particle interaction models predict losses through pitch-angle scattering into the atmospheric loss cone is the direct comparison between the ionization altitude profiles expected in the atmosphere due to the precipitating fluxes and the ionization profiles actually measured with incoherent scatter radars. This paper reports such a comparison using a forward propagation of loss-cone electron fluxes, calculated with the electron pitch angle diffusion model applied to Van Allen Probes measurements, coupled with the Boulder Electron Radiation to Ionization (BERI) model, which propagates the fluxes into the atmosphere. The density profiles measured with the Poker Flat Incoherent Scatter Radar operating in modes especially designed to optimize measurements in the D-region, show multiple instances of quantitative agreement with predicted density profiles from precipitation of electrons caused by wave-particle interactions in the inner magnetosphere. There are two several-minute long intervals of close prediction-observation approximation in the 65-93 km altitude range. These results indicate that the whistler wave-electron interactions models are realistic and produce precipitation fluxes of electrons with energies between 10 keV to >100 keV that are consistent with observations.

**Plain language summary**

Establishing how electromagnetic waves in the magnetosphere push high-energy electrons into a funnel directed toward Earth along magnetic field lines is a critically important step to predict how electrons are lost into the atmosphere during geomagnetic storms.

Wave-electron interaction models predict the number of electrons that are funneled toward Earth from a set of in-situ spacecraft measurements. As the electrons hurl into the upper atmosphere, ionization models predict how many electrons would be released by the neutral atmosphere due to the bombardment from funneled electrons. Electron density measurements with a radar especially tuned to optimize detection of electron densities in the upper atmosphere can be compared to predicted electron densities to determine the validity of the electron loss models. This paper reports a comparison for an interval of time when a Van Allen Probe spacecraft is measuring the waves and electrons at a location that would guarantee that the electrons would fall near the radar's location in Poker Flat, Alaska. The comparison shows that the models considered predict the correct number of electrons in multiple instances, thus establishing an important step in verifying the validity of the models of electron loss during geomagnetic storms.

## 1. Introduction

One of the most important and challenging issues in radiation belt physics at the present time is understanding the balance between acceleration of electrons up to relativistic energies and losses out of the system. The precipitation of energetic electrons from the radiation belts into the atmosphere is one of the most important loss mechanisms. It acts as a regulator of radiation belt energy fluxes and, when penetrating into the atmosphere, causes compositional changes to the lower thermosphere, mesosphere and upper stratosphere (e.g., Turunen et al., 2009; Millan et al., 2013).

Current theories of particle precipitation assume that energetic particles in the magnetosphere precipitate into the atmosphere after undergoing pitch-angle scattering into the loss cone due to interactions with plasma waves near the geomagnetic equator (e.g., Thorne, 2010; Millan and Thorne, 2007; Millan et al., 2013). Several plasma waves are known to be able to scatter electrons into the atmospheric loss cone through pitch angle diffusion. Three wave modes are considered to be particularly dominant in driving this scattering, namely extremely-low- to very-low frequency (ELF/VLF) whistler-mode chorus, ELF/VLF plasmaspheric hiss and electromagnetic ion-cyclotron (EMIC) waves (e.g., Millan and Thorne, 2007). Whistler-mode chorus waves are discrete whistler emissions observed outside the plasmasphere in the frequency range between the lower hybrid and the electron cyclotron frequencies, $f_{\mathrm{LHR}} - f_{ce}$ (~100 Hz–10 kHz), where $f_{\mathrm{ce}}$ and $f_{\mathrm{LHR}}$ are equatorial electron gyrofrequency and the lower hybrid resonance frequency, respectively. Waves generated at the equator pitch-angle scatter 0.1-1 keV electrons that generate diffuse aurora (Thorne et al., 2010) and $\gtrsim$10 keV electrons that generate pulsating aurora (Nishimura et al., 2010). Waves propagating to higher latitude pitch-angle scatter electrons with ~100 keV to 1 MeV energies (Lorentzen et al., 2001; Horne and Thorne, 2003). Chorus waves are thus expected to cause electron precipitation over a wide range of energies (Ma et al., 2020). Plasmaspheric hiss is a broadband ELF (100 Hz-few kHz) whistler mode emission occurring mostly in the high-density plasmasphere and drainage plumes (Thorne et al., 1973). EMIC waves can occur in three distinct bands: hydrogen band between the He+ and H+ gyrofrequencies, helium band between the O+ and He+ gyrofrequencies, and oxygen band below the O+ gyrofrequency. EMIC waves are theorized to efficiently scatter relativistic electrons into the loss-cone through Doppler-shifted resonances (Albert, 2003; Summers and Thorne, 2003). The importance of EMIC waves as a scattering source of outer radiation belt relativistic electrons has been demonstrated although the scattering efficiency could strongly depend on the modeling parameters (e.g., *Zhang et al.*, 2016; *Ross et al.*, 2020).

Experimental verification of the electron atmospheric loss has been focused on correlative studies using particle and optical measurements from the ground, or particle measurements at low-altitude orbit, and in-situ measurements of waves and particles in the inner magnetosphere. Several case studies have revealed a close correlation between electron precipitation, visualized using measurements from ground-based optical cameras, and chorus waves, measured near the inner-magnetosphere equator (Nishimura et al., 2010; Kasahara et al., 2018; Ozaki et al., 2019). Other studies have established correlation between low-altitude spacecraft observations of electron precipitation and observations of chorus waves near the equator (Lorentzen et al., 2001; Breneman et al., 2017). Studies coordinating ground-based riometers or balloon-mounted X-ray detectors with spacecraft observations have established correlation between chorus waves and Bremsstrahlung X-ray emissions in the upper atmosphere (Rosenberg et al., 1971; Millan et al., 2013). Observations of microbursts with low-orbiting spacecraft, coincident with chorus observations near the equator have demonstrated a direct link between relativistic electron microbursts and chorus waves (Mozer et al., 2018; Breneman et al., 2017).

EISCAT Tromso Incoherent scatter radar (ISR) measurements of density in the lower ionosphere, coordinated with Van Allen Probes measurements of waves and particles were carried out by Miyoshi et al. (2015) to determine whether there is a correlation between the chorus-induced loss-cone flux of electrons near the equatorial inner magnetosphere and the electron density observed in the ionospheric D- and E-regions, between ~68 km and ~190 km. Qualitative similarity between the electron energy spectra in the energy range between ~10 of keV and ~100 keV, inferred from ISR observations averaged over a 22-minute interval, and the averaged spectra observed with Van Allen Probe-A suggests that the magnetospheric electron population fills the loss-cone under the strong-diffusion limit. Similarity between the same ISR-inferred energy spectra and the spectra predicted by the by a test-particle simulation scaled to match Van Allen Probe's particle measurements at the launch point, suggests that whistler chorus is responsible for the observed lower-energy portion of the energy spectra of precipitating electrons.

This communication presents the first direct quantitative comparison between the ISR-measured electron density profiles and the electron density profiles predicted by a forward electron transport model that propagates the loss-cone flux, launched by the whistler-electron interaction near the magnetospheric equator, from the topside ionosphere down to the D-region. The wave-particle interaction that predicts the topside precipitating flux is calculated by applying the UCLA wave-particle Full Diffusion Code to Van Allen Probe particle and wave measurements. The density measurements were made with an incoherent scatter radar mode optimized for the estimation of spectra in the collision-dominated D-region ionosphere, capable of measurements with sub-kilometer spatial resolution and ~1-minute temporal resolution.

The paper is organized as follows. Section 2 describes the three-step method of analysis. Section 3 describes the characteristics of the storm event where the conjunction develops. Section 4 describes the results of the comparison between observed and predicted density profiles. Section 5 discusses the implications of the comparisons.

## 2. **Method of Analysis**

The comparison of PFISR-observed profiles with predicted profiles in each conjunction interval is achieved with a three-step procedure. The first step is the calculation of loss-cone electron flux using the UCLA wave-particle Full Diffusion Code, propagated to the ionosphere at 500 km. The second step is the calculation of the electron density produced by the precipitating flux as a function of altitude using the Boulder Electron Radiation to Ionization (BERI) model. In the final step the electron density altitude profiles observed with the Poker Flat ISR (PFISR) are compared with the electron density profiles predicted with the BERI model.

**Electron Precipitation Modeling**. In the first step, we use the Van Allen Probes observations and quasi-linear theory to model the electron loss-cone fluxes driven by whistler mode chorus waves near the equatorial magnetosphere. The Helium Oxygen Proton Electron (HOPE) plasma spectrometer (Funsten et al., 2013) and the Magnetic Electron Ion Spectrometer (MagEIS) (Blake et al., 2013) instruments measure the electron fluxes at 15 eV – 50 keV energies and ~4.5° – 90° pitch angles, and the fluxes at 33 keV – 4 MeV energies and ~8° – 90° pitch angles, respectively. The Electric and Magnetic Field Instrument Suite (EMFISIS) instrument (Kletzing et al., 2013) measures the wave electric field and magnetic field intensities and background magnetic fields. The double-probe electric field instrument obtains two data components perpendicular to the spin axis of the satellite and one component parallel to the spin axis, ranging in frequency from DC to

400 kHz. The magnetometer data has two frequency regimes: the fluxgate, which has frequency coverage from DC to 32 Hz, and the triaxial search coil, which can cover frequencies up to 12 kHz. Both magnetometers are in the same frame of reference as the electric field instruments. The whistler-mode waves are measured by the Waveform Receiver (WFR) at frequencies from ~10 Hz to 12 kHz. The wave polarization properties are provided through the Singular Value Decomposition method, including the wave normal angle, ellipticity, planarity, and degree of polarization. The total electron density is inferred by identifying the upper hybrid resonance frequency line measured by the High Frequency Receiver (Kurth et al., 2015). We automatically select the whistler mode waves by requiring the wave ellipticity to be higher than 0.7 and degree of polarization to be higher than 0.7. During the event analyzed in this paper, the quasi-parallel and oblique wave components are selected by requiring the wave normal angle to be smaller and higher than 45°, respectively, to account for the different properties of the two groups of chorus waves.

The bounce-averaged diffusion coefficients are calculated using the UCLA Full Diffusion Code (Ni et al., 2008, 2011), at each time of the whistler mode wave observation by Van Allen Probes. The wave frequency spectrum is obtained from the selected chorus wave intensities. The Van Allen Probes observation of background magnetic field and total electron density are used in the diffusion coefficients calculations. We assume that the wave normal angle distribution follows a Gaussian function, i.e., proportional to exp $(-(\frac{\tan\theta-\tan\theta_m}{\tan\theta_w})^2)$, where $\theta_{min} \le \theta \le \theta_{max}$, at the latitude range from equator to the maximum latitude $\lambda_{max}$. For quasi-parallel propagating chorus waves, we assume that $\theta_m = 0°$, $\theta_w = 30°$, $\theta_{min} = 0°$, $\theta_{max} = 45°$, and $\lambda_{max} = 30°$; for oblique chorus waves, we assume $\theta_m = 65°$, $\theta_w = 30°$, $\theta_{min} = 45°$, $\theta_{max} = 75°$, and $\lambda_{max} = 10°$. Ten orders of harmonic resonances and Landau resonance are considered ($-10 \le N \le 10$, where $N$ is the harmonic number). We also consider the electron scattering due to Coulomb collision with atmospheric molecules and charged particles (*Abel and Thorne,* 1998).

Assuming a quasi-equilibrium pitch angle distribution of electrons, the ratio between the average electron flux inside the loss cone and the flux just outside the loss cone ($\chi(E) = J_{prec}/J_{out}$) can be estimated using the bounce-averaged pitch angle diffusion coefficient at the loss cone ($\langle D_{\alpha\alpha}\rangle_{LC}$) and the strong diffusion rate ($D_{SD} = 2 \cdot {\alpha_{LC}}^2/\tau_B$) as:

$$\chi(E) = \frac{2\int_0^1 I_0[Z_0 \cdot \tau] \cdot \tau \cdot d\tau}{I_0[Z_0]}, \tag{1}$$

where $Z_0 = \sqrt{D_{SD}/\langle D_{\alpha\alpha}\rangle_{LC}}$ , $\alpha_{LC}$ is the pitch angle at the bounce loss cone, $\tau_B$ is the bounce period, $I_0$ is the modified Bessel function of the first kind, and $\tau$ is an integration variable. The ratio $\chi(E)$ is defined as the loss cone filling index after *Ni et al.* (2014). The energy spectrum of precipitating electron flux ($J_{\text{prec}}$) is obtained using the loss cone filling index and the flux just outside the loss-cone ($J_{\text{out}}$) obtained from observation. The characteristic precipitating energy $E_c$ is calculated as:

$$E_c = \frac{\int_{E_{min}}^{E_{max}} J_{prec} \cdot E \cdot dE}{\int_{E_{min}}^{E_{max}} J_{prec} \cdot dE}. \tag{2}$$

The total precipitating energy flux at the ionosphere is

$$Q = \pi \int_{E_{min}}^{E_{max}} J_{prec} \cdot E \cdot dE \quad , \tag{3}$$

following Liang et al. (2011) and Clark et al. (2018). The modeled average precipitating flux of electrons ($J_{\text{prec}}$) is mapped to 500 km altitude. We assume an isotropic electron pitch angle distribution within the pitch angle of loss cone, due to the large pitch angle diffusion coefficients induced by intense whistler mode wave scattering and Coulomb collision. The pitch angle scattering rate due to Coulomb collision inside the loss cone is larger or comparable to the strong diffusion limit at energies below tens of keV at L = 6. Ma et al. (2021) has shown the consistency between the calculated $J_{prec}$ and results from Fokker Planck simulation, after a quasi-equilibrium state of electron pitch angle distribution is formed near the loss cone.

**Ionization Modeling.** The second step of the procedure is to determine the ionization profiles in the E- and D-region caused by fluxes and spectra of loss-cone electrons propagated from the VAP location along the magnetic field to 500 km altitude. The energy and pitch angle distribution of precipitation fluxes determined from the first step are used to calculate the ionization production using the Boulder Electron Radiation to Ionization (BERI) model (Xu et al., 2020). This model is largely based on a lookup table of atmospheric ionization production by monoenergetic electrons with energies between 3 keV and 33 MeV, and pitch angles between 0° and 90°. This lookup table was developed using physics-based Monte Carlo simulations (Lehtinen et al., 1999), and allows rapid and accurate specification of ionization production by arbitrary precipitation energy and pitch angle distribution in any atmospheric condition. The mass density profile of background atmosphere is calculated using the NRLMSISE-00 model (Picone et al., 2002) for the date, latitude and longitude of PFISR measurements.

After obtaining the ionization production using the BERI model, we simulate the electron density change at altitudes below 150 km using the Glukhov, Pasko, and Inan (GPI) chemistry model. The GPI model is a five-species model that includes electrons, heavy and light positive ions, and heavy and light negative ions (Lehtinen and Inan, 2007). This model has been extensively used in studies related to D-region electron density changes due to transient luminous events or radiation belt precipitation (e.g., Marshall et al., 2019). Although simplified using five species, this model, in general, provides consistent results with the Sodankylä Ion Chemistry (SIC) model

(Marshall et al., 2019). The background ionosphere used in GPI simulation is calculated using the International Reference Ionosphere (IRI) model (Bilitza, 2001), at the date, latitude, and longitude of PFISR measurements.

**PFISR-BERI Comparison.** The third step is the direct comparison between the electron density profiles inferred with the transport model and the E- and the D-region electron density profiles measured with the Incoherent Scatter Radar located at the Poker Flat Research Range (65.13º N, 147.47º W). PFISR is a remotely operated, phased-array radar with pulse-to-pulse steering capability (Nicolls et sl., 2007; Heinselman and Nicolls, 2008). During expected VAP-PFISR conjunction events, the radar is operated in modes optimized for the estimation of spectra in the collision-dominated D-region ionosphere. The spectrum in this regime can be represented as a Lorentzian distribution with increasing spectral width and amplitude as a function of altitude (Dougherty and Farley, 1963; Mathews, 1978; Nicolls et al., 2010). For typical D-region parameters the spectral width of this type of distribution is between tens and hundreds of Hz, which is much narrower than kHz bandwidths in the E- and F-region. The narrow bandwidth, which corresponds to a long decorrelation in the time domain, combined with the proximity of the ionospheric target region (~50-100 km) makes possible the application of pulse-to-pulse radar processing schemes. The observations reported here use a 13 baud, 10 μs baud barker code oversampled at 5 μs (750 m spatial resolution). The experiment uses a 2 ms inter-pulse period (IPP), meaning the pulse-to-pulse spectra have a Nyquist limit of 250 Hz, and spectra are processed using zero-padded periodograms of 128 pulses (3.9 Hz spectral resolution). The ion-line ISR spectrum can only be observed when the radar's Bragg wavelength is long compared to the electron Debye length, and for PFISR operating frequency of 449.3 MHz and a typical D-region electron temperature of 200 K this limit is encountered at densities of ~$3 \times 10^2$ $cm^{-3}$. In practice PFISR does not have sufficient sensitivity to detect densities down to the Debye length limit, and the detection limit varies between $10^3$ $cm^{-3}$ and $10^4$ $cm^{-3}$ depending on the spectral width and target range, with narrower-bandwidth and shorter-range targets being easier to detect. Above ~90 km altitude, frequency aliasing prevents estimation of the spectrum using pulse-to-pulse processing, but the total scattered power can still be measured. The D-region mode used for this study uses four beam positions: vertical, magnetic-field-aligned, and two outrigger beams pointed northwest and east-north-east, respectively. The magnetic-field-aligned beam measurements are used in the present comparisons because the orientation of this beam is closest to the foot-point of both Van Allen Probes' orbits at the time of the conjunction.

## 3. VAP-PFISR Conjunction of May 8, 2018

The event of interest involves a conjunction between PFISR and both Van Allen Probes in the pre-dawn sector. During the entire conjunction both Van Allen Probes were near their respective orbit apogee and remained in close proximity to each other, with Probe-B sampling the same L-shell and similar MLT approximately 30 minutes ahead of Probe-A during 1400-1600 UT (Figure 1). The radar's location projects to a magnetospheric equatorial location of L~5.3, ~6.2 $R_e$ or ~6.9, depending on the application of the T89, T02 or T96 Tsyganenko magnetic field models respectively (Tsyganenko, 1989, 1996, 2002) for the moderate storm conditions observed on May 8, 2018 (3 nPa dynamic pressure, 600 km/s solar wind speed, Dst = -30 nT, Kp = 2). Depending on the mapping used, the radar location's projection is either ~1 $R_e$ closer to Earth or ~0.5 $R_e$ farther from Earth than the apogee of the Van Allen Probes ($L$ ~ 6.4). The closest proximity between the probes' foot-points and PFISR's field-aligned beam at 100 km altitude is ~300 km, achieved at 1430 UT for VAP-B, and ~350 km at 1445 UT for VAP-A. However, the situation reverses after ~1445 UT when VAP-B's foot-point starts to have a broader separation from PFISR than VAP-A.

The conjunction occurred during a storm caused by a high-speed solar stream and started with a sudden impulse at 1030 UT on May 5 (Figure 2). The storm continued for several days, during which the solar wind speed stayed at ~600 km/s. The SuperMAG Ring current (SMR) index reached a minimum of -65 nT at the beginning of May 6 and multiple recurring westward electrojet intensifications with SML < -500 nT. The PFISR-VAP conjunction interval occurred during the storm recovery and was embedded in an interval of westward electrojet intensification with a minimum SML (lower envelope of the SuperMAG Auroral Electrojet index) value of -800 nT (Figure 3).

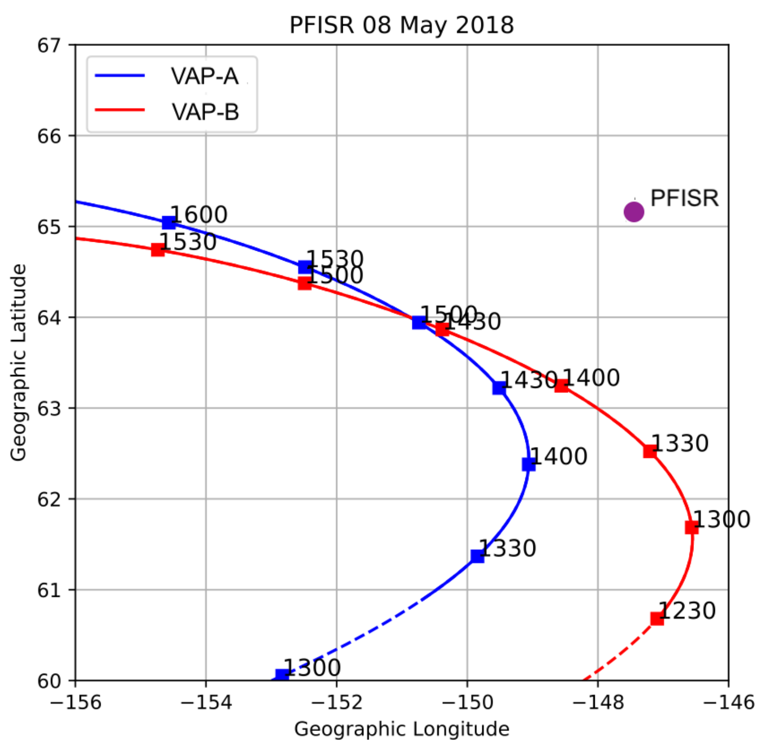


**Figure 1.** Track of VAP orbits' foot-points relative to PFISR vertical beam at 100 km altitude in geographic coordinates.

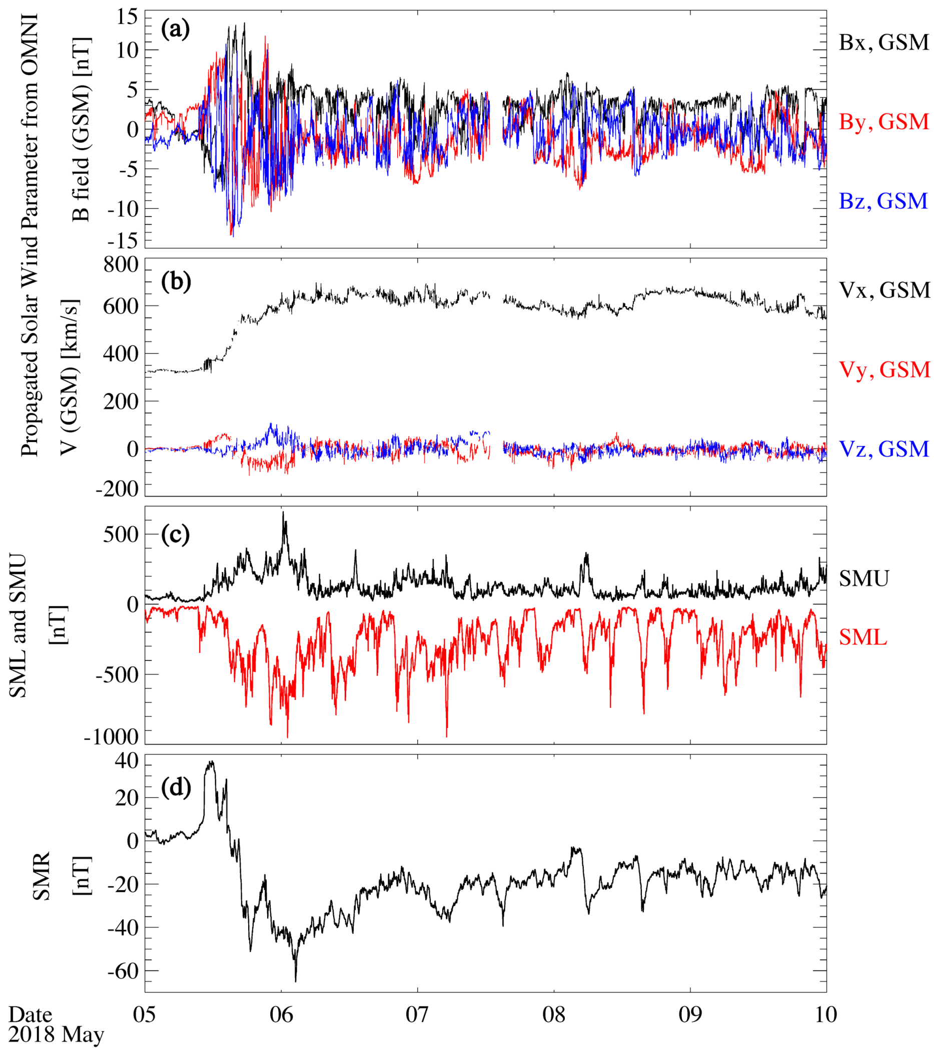


**Figure 2.** Interplanetary magnetic field (a), solar wind parameters (b), SME U/L indices (c) and SMR index (d) during the high-speed streamer storm that started on 5 May, 2018.

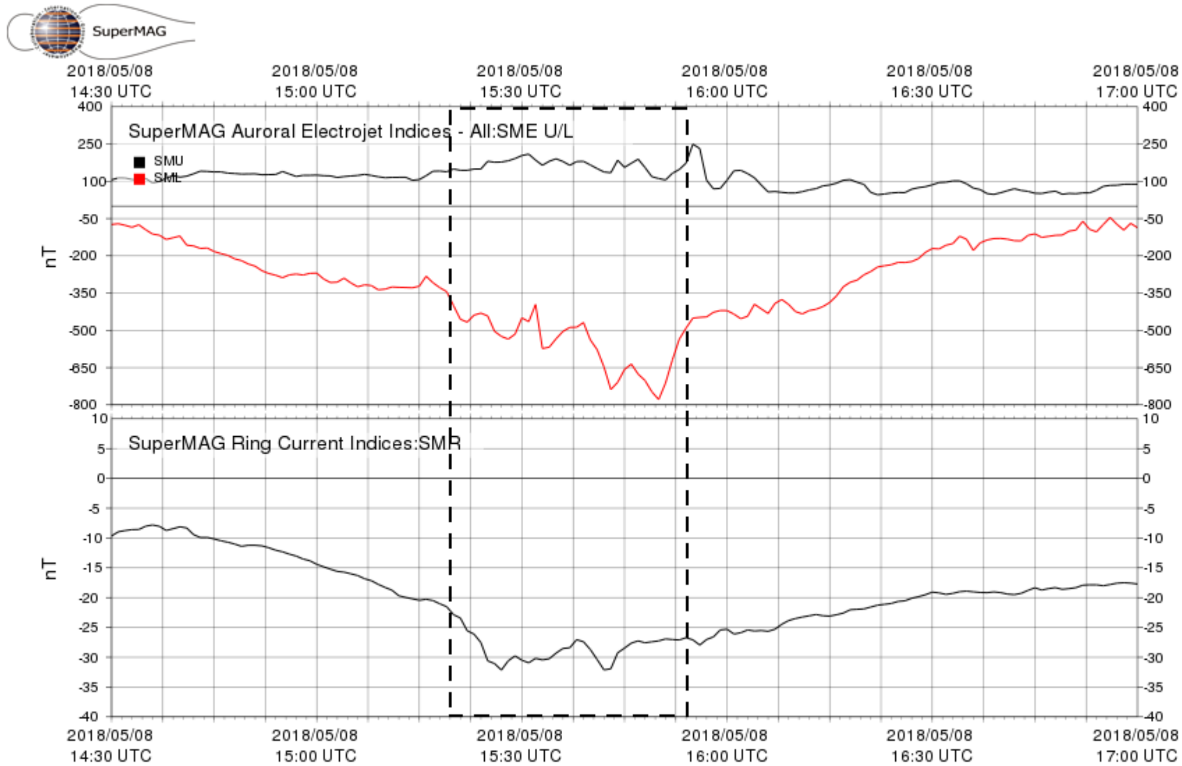


**Figure 3.** SME U/L indices (top panel) and SMR index for the PFISR-VAP conjunction period of 8 May, 2018. The dashed box indicates the span of the PFISR-VAP conjunction interval analyzed.

The Van Allen Probes were located outside the plasmapause as indicated by the low total electron densities (1–3 cm$^{-3}$) observed during 1430 – 1700 UT (Figures 4a and 4h). Figures 4b and 4i show that the chorus waves observed by both VAP spacecraft are very similar to each other. Whistler wave activity in the frequency range from 200 Hz to approximately 2 kHz was observed between 1510 UT and 1640 UT on both spacecraft. The wave power is concentrated in two bands. One at approximately 1 kHz, which is below one half the equatorial electron cyclotron frequency at VAP's location, and another that starts at 300 Hz and shifts to higher frequency until it merges with the first band toward 1555 UT. The chorus waves are quasi-field-aligned with wave normal angles mostly below 30° (Figures 4c and 4j), except for an oblique wave burst observed during 1525 – 1540 UT at ~1 kHz. For the quasi-parallel propagating chorus waves, we selected the most intense chorus wave power that is expected to effectively precipitate electrons by requiring the wave ellipticity to be higher than 0.7, degree of polarization higher than 0.7, wave normal angle lower than 45°, and wave intensity larger than $10^{-8}$ $nT^2/Hz$. The oblique propagating chorus waves were selected using the same criteria except for requiring the wave normal angle higher than 45°.  The largest amplitude of chorus waves reached above 10 pT over all but a few minutes, and peaks above 100 pT intermittently over several minutes, in the interval between 1520 UT and 1555 UT for both spacecraft (Figures 4d and 4k). This interval is the focus of the comparison between predicted and observed electron density profiles.

The pitch angle diffusion coefficients of electrons (Figures 4e and 4l) are calculated using the observed chorus wave frequency spectra. Since the intense chorus waves with small wave normal angles are observed at ~10° magnetic latitude, we assumed that the latitude range of quasi-parallel propagating chorus waves is between the equator and 30°. The latitude range of oblique chorus waves is assumed to be between the equator and 10°. The bounce-averaged diffusion coefficients reach ~0.1 $s^{-1}$ when chorus waves are strong, exceeding the strong diffusion limit near the energies of electron cyclotron resonance (e.g., ~50-100 keV energy during 1530-1540 UT observed by Probe A).

The energy spectrograms of electron fluxes (Figures 4f and 4m) show significant flux enhancement with clear energy dispersion at 20 – 200 keV energies, indicating an electron injection event occurring simultaneously with chorus wave intensification. The energy spectrum of precipitating electron flux (Figures 4g and 4n) is modeled using the observed electron flux and the diffusion coefficients at the loss cone pitch angle. The most significant electron precipitation is modeled during 1520 – 1555 UT, and the energy of precipitation varies with the wave frequency. In general, the chorus waves at ~1 kHz cause the electron precipitation at ~20 – 40 keV energies, and the waves at ~300 – 600 Hz cause the precipitation at ~60 – 200 keV energies.

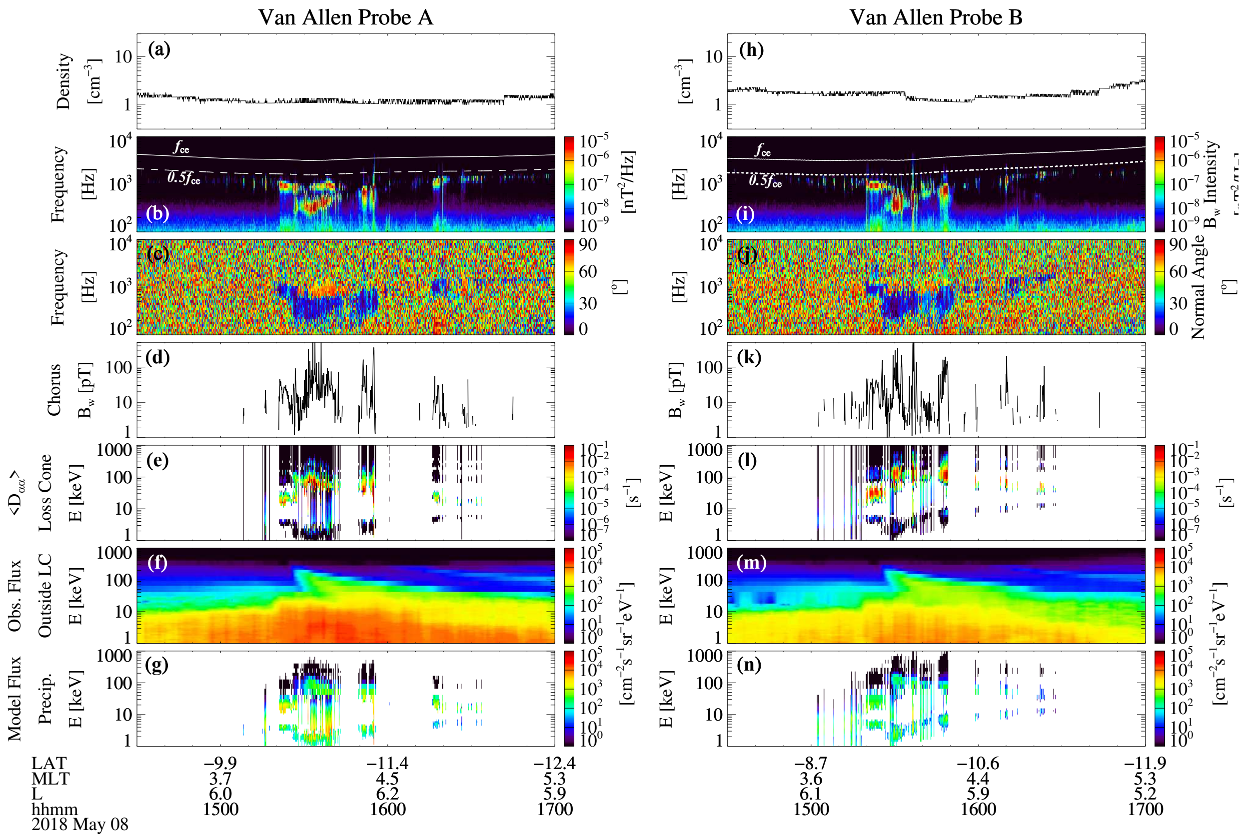


**Figure 4.** VAP-A measurements of (a) total electron density inferred from the upper hybrid line in the HFR spectrogram, (b) magnetic field power spectra with white solid and dashed lines representing equatorial electron gyrofrequency ($f_{ce}$) and $0.5f_{ce}$, (c) wave normal angle, (d) chorus wave amplitude, (e) pitch angle diffusion coefficients at the equatorial pitch angle of the bounce loss cone in the 1-1,000 keV energy range, (f) electron flux in the 1-1,000 keV energy range using HOPE below 30 keV and MagEIS above 30 keV, (g) modeled precipitating electron flux from 1-1,000 keV using the UCLA full diffusion code. (h-n) VAP-B particle and wave measurements and the diffusion modeling results for the same time interval and format.

## 4. PFISR-UCLA-BERI Comparisons

Figure 5 shows a comparison between the estimated electron density ($N_e$) at altitude $h$ obtained from fitting the PFISR spectra (top panel) and the $N_e$ predicted from the UCLA-BERI forward propagation for VAP-A (bottom panel), in the entire conjunction interval.

Figure 5 (top) shows the estimated electron density obtained from fitting the PFISR spectra. In the collision dominated D-region the incoherent scatter spectrum becomes Lorentzian with a spectral width that is inversely proportional to the ion-neutral collision frequency [Nicolls et al. 2010]. The spectra become exponentially narrower with decreasing altitude, which enables easier detection of low electron densities at lower altitudes. The fitting procedure uses a Levenberg-Marquardt nonlinear least squares algorithm to estimate four parameters for each altitude: electron density ($N_e$), line-of-sight Doppler velocity ($V_D$), spectral width ($\gamma$), and the noise level ($N$). The procedure fits all altitudes simultaneously, and the noise levels are regularized to be close to an a priori measured noise from long ranges. Fitting for the noise level allows the algorithm to compensate for small range-dependent noise contributions in the radar, range-aliased F-region returns, and broad-band interference. Furthermore, the algorithm uses the full covariance matrix of the calculated spectrum and propagates that covariance into the a-posteriori error estimates of the fitted parameters. After fitting the incoherent scatter spectra we filter the results based on heuristic acceptance criteria that indicate genuine detections of a Lorentzian IS spectrum. We accept points where $N_e > 2\sigma_{Ne}$ and $\gamma > 1\sigma_\gamma$ , where $\sigma_{Ne}$ and $\sigma_\gamma$ are the a-posteriori errors of the electron density and spectral width, respectively. The first criterion rejects points that are too small to be statistically significant compared to zero electron density, and the second criterion rejects fits with extremely small spectral widths where the algorithm has likely converged to a local minimum and fit a single point in the digital frequency domain, which is a common problem when fitting Lorentzian spectra to noise-like data. The white regions in Figure 5 (top) where the fit results have been rejected indicate regions where the electron density is too small for PFISR to reasonably detect.

A visual comparison between PFISR observations and UCLA-BERI models' prediction shows the same trends in the properties of the precipitation region. The energetic electron precipitation, characterized by $N_e$ distributions reaching below 80 km altitude, is seen at the onset of energetic precipitation, at 1526 UT, and a nearly monotonic tapering off to lower precipitation energies thereon until 1630 UT, when precipitation occurs above the 93 km upper limit of the PFISR D-region mode.

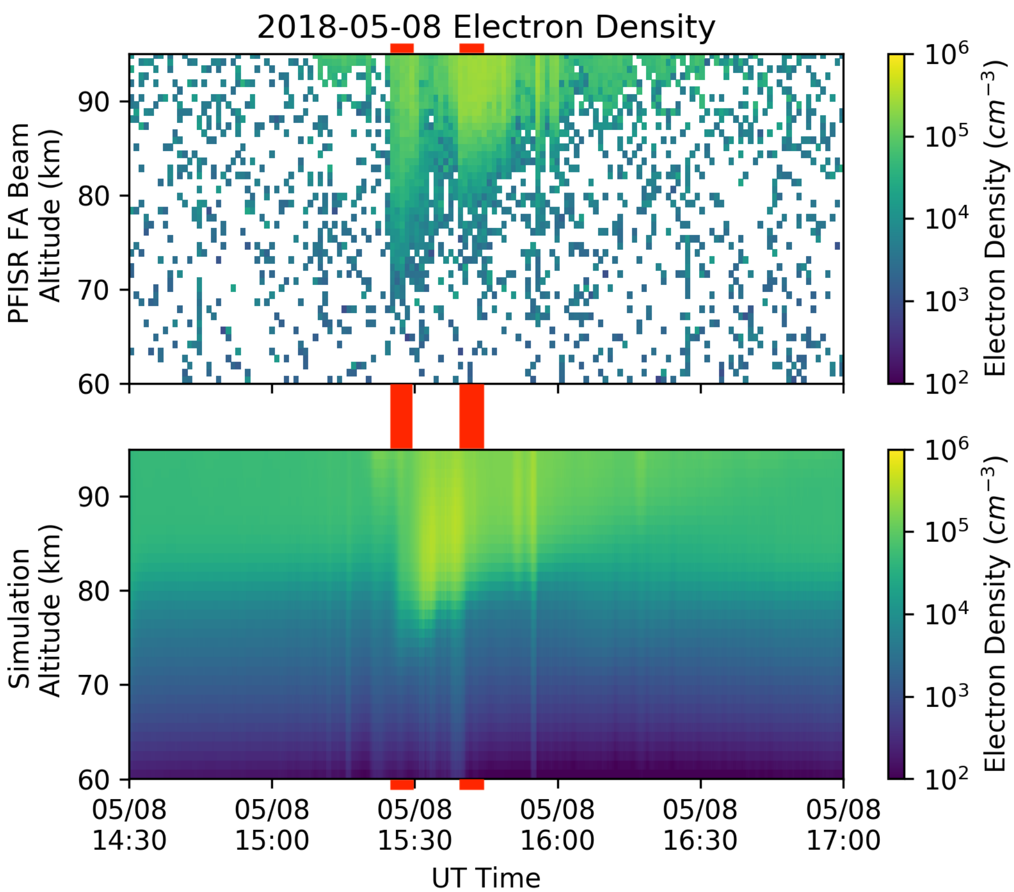

**Figure 5.** Altitude profiles of electron density measured with the field-aligned PFISR beam (top panel) and UCLA-BERI-modeled altitude profiles (bottom panel) during the PFISR-VAP-A conjunction period of 8 May, 2018. The left-side set of red bars indicates the time interval with PFISR-BERI-UCLA comparisons in Figure 6. The right-side set of bars is the time interval for comparisons in Figure 8.

A direct model-data comparison for the first two $N_e(h)$ 1-minute profiles bracketing the 1526 UT onset of energetic precipitation is shown in Figure 6. Every PFISR 1-minute averaged $N_e(h)$ profile in the conjunction is compared with consecutive 1-minute averaged $N_e(h)$ UCLA-BERI profiles encompassing ten minutes before and after the PFISR profile until the closest agreement is found for the height range 80 km $< h <$ 93 km and the height range 54 km $< h <$ 80 km. The ten-minute criterion allows for a 500 m/s convection in the ionosphere to transport the electron precipitation region the 300 km distance that separates the foot-point of VAP-A from the PFISR field-aligned beam. The boundary separating the two altitude regimes is chosen because above 80 km the plasma is dominated by electrons and simple positive ions, but below 80 km the composition transitions to mostly positive cluster ions and negative ions, with free electrons becoming a minor species (Glukhov, 1992; Lehtinen and Inan, 2007). Since the 80 km altitude is the peak ionization altitude for 100 keV precipitating electrons (e.g., Xu et al., 2018), it can also be used to separate the high-energy population from the lower energy plasma sheet electron population, which precipitates at higher altitudes.

For the PFISR profile starting at 1525:23 UT (Figure 6, top left panel), the UCLA-BERI's results that show best agreement down to 76 km are at 1526:48 UT, after applying model-data comparison between the 1-minute PFISR integration and every 1-minute model- predicted profile in the ±10-minute window. The agreement degrades for the higher energy precipitation, corresponding to altitudes between 70 and 76 km. The measured density is ~4.5 times as large as the expected density at 71 km for VAP-A. The high-energy model-data discrepancy is significantly reduced for the 1527:25 PFISR profile and its best agreement from the models' results of 1527:18 UT (Figure 6, top right panel). The discrepancy is reduced to a layer between 71 and 74 km. The observed density is ~3 times the predicted density at 72 km. Subsequent modeled 1-minute profiles maintain good approximation to observations. The 1528:26 UT PFISR profile (Figure 6 bottom left panel) is best approximated by the modeled precipitation from 1526:48 UT between 68 km and 82 km. But in the 82-93 km altitude layer the observed $N_e$ is larger than the model-predicted $N_e$. It is as much as ~58% larger at 87 km for VAP-A. The discrepancy is reduced to ~48% and to the 84-88 km altitude layer in the next 1-minute profile (Figure 7, bottom right panel), although the profile approximation is slightly degraded below ~74 km.

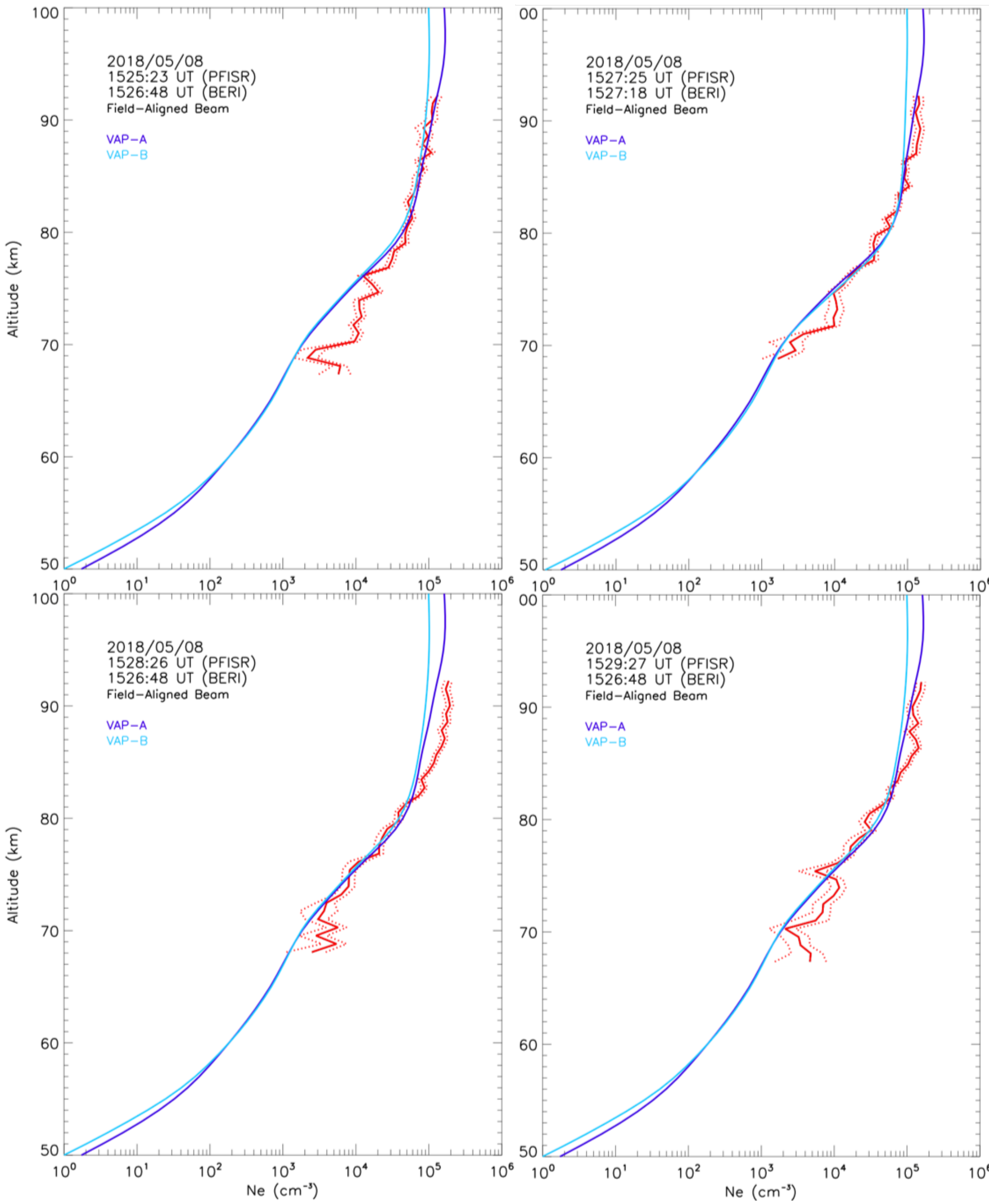


**Figure 6.** Altitude profiles of electron density measured with the field-aligned PFISR beam (red line) at 1525:23 UT (left top panel), 1527:25 UT (right top panel), 1528:26 UT (bottom

left panel), and 1529:27 UT. UCLA-BERI-modeled altitude profile for VAP-A (dark blue) and VAP-B (light blue) at the start of the energetic particle precipitation interval. Red dotted lines indicate one standard deviation above and below the observed $N_e(h)$.

The model-data discrepancy becomes more pronounced for all subsequent altitude profiles between 1529:42 UT and 1537:34 UT, with PFISR-measured densities significantly smaller than predicted for all sampled altitudes, as shown in Figure 5. In that interval PFISR is inside a region of depleted electron density while both VAP spacecraft are in a region that generates an electron density peak at ~83 km that is not reproduced by any of the PFISR $N_e$ profiles measured within the sliding ±10-minute window that would fit any convection delays or drift front geometries. The predicted density shows an intense peak between ~$2x10^5$ $cm^{-3}$ and ~$4x10^5$ $cm^{-3}$ over an altitude between ~83 and ~85 km which is not reproduced in the PFISR measurements during the entire density depletion period. Figure 7 shows the UCLA-BERI-predicted density profile at 1536:34 UT, with a peak altitude of 85 km and a density of $3.5x10^5$ $cm^{-3}$. The observed density is lower at every measured altitude (becoming over one order of magnitude smaller at 85 km) and the density peak is at least 7 km higher.

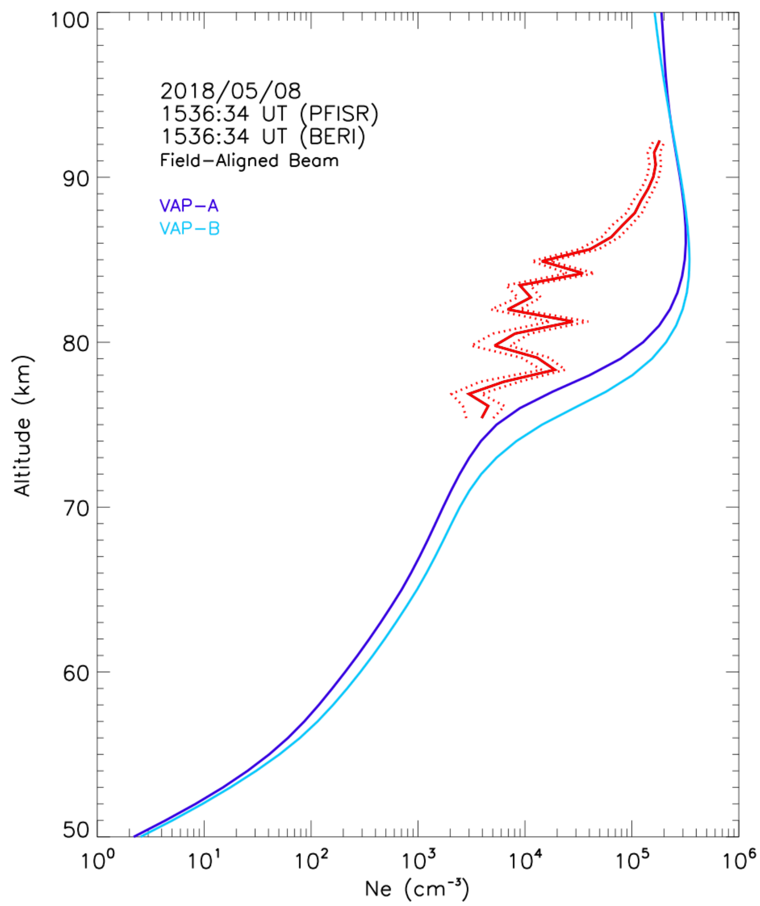


**Figure 7.** Altitude profiles of electron density measured with the field-aligned PFISR beam (red line) at 1539:36 UT (left panel) and 1536:34 UT, and UCLA-BERI-modeled altitude profile for VAP-A (dark blue) and VAP-B (light blue). Red dotted lines indicate one standard deviation above and below the observed $N_e(h)$.

Model-observation agreement becomes stronger after 1537:34 UT and remains so for the remainder of the observation period. At 1539:36 UT, for instance, the PFISR-observed profile matches UCLA-BERI-predicted profile below 80 km and above 85 km (Figure 8, left panel). For the intermediate altitudes the observed density shows a deficit of ~50-60% near the peak of the profile. However, subsequent profiles show a close model-observation agreement over a wider range of altitudes, as can be seen in the 1544:38 UT comparison (Figure 8, right panel), where the good fit extends between 71 km and 93 km, with the exception of a 77-80 km altitude layer where PFISR-measured density is 1.5 times smaller than the modeled density, and an 88-93 km layer, where PFISR-measured density is 35% larger than the modeled density.

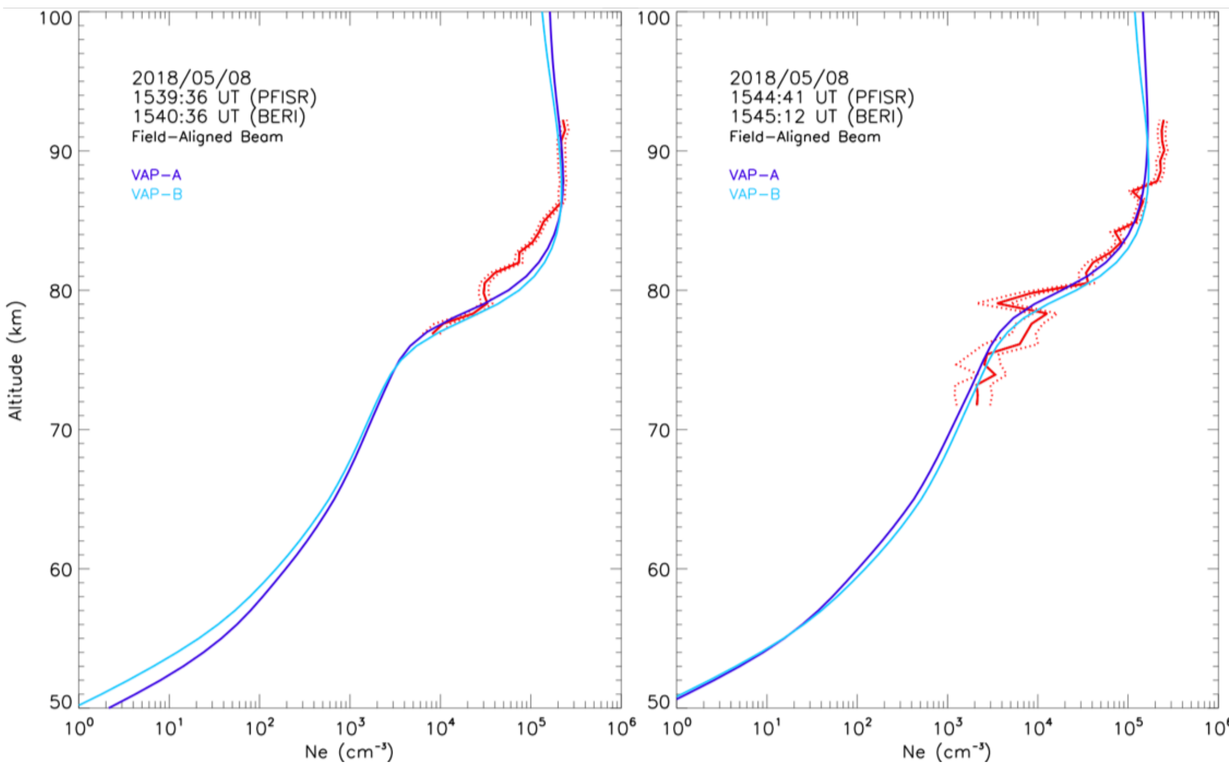


**Figure 8.** Altitude profiles of electron density measured with the field-aligned PFISR beam (red line) at 1539:36 UT (left panel) and 1544:41 UT, and UCLA-BERI-modeled altitude profile for VAP-A (dark blue) and VAP-B (light blue). Red dotted lines indicate one standard deviation above and below the observed $N_e(h)$.

## 5. Discussion and Conclusion

This communication reports the first direct comparison between the ionization altitude profiles expected in the atmosphere due to energetic electron precipitation and the ionization profiles measured with incoherent scatter radars. The comparison is performed using a forward propagation of loss-cone electron fluxes, calculated with the UCLA wave-particle model applied to Van Allen Probes measurements, into the topside ionosphere and transported into the atmosphere with the BERI model.

The principal result of the prediction-observation comparison is that density profiles measured with PFISR show multiple instances of quantitative agreement with predicted density profiles from precipitation of electrons caused by whistler wave-electron interactions in the inner magnetosphere.

There are two intervals between ~1524 UT (the onset time of high-energy electron precipitation commences) and ~1550 UT (the time when precipitation recedes above the upper boundary of sensitivity of the PFISR D-region mode) where close approximations of UCLA-BERI-predicted electron density profiles and PFISR-measured density profiles are apparent in the entire altitude regime between ~65 km and ~93 km, indicating that the rates of diffusion into the loss-cone predicted by the UCLA Full Diffusion Code produce the necessary amount of flux for all energies between several tens to several hundreds of keV to match the ionization profiles observed at those altitudes by PFISR. Good model-observation agreement is apparent despite the assumptions embedded in the models and the spatial separation between the field-of-view of the field-aligned PFISR beam and the ionospheric projections of the Van Allen Probes' locations at the time of the observations.  There are several intervals in the observation period that show a close prediction-observation agreement over nearly the entire range of altitudes sampled (see bottom panels of Figures 6, 7 and 8) indicating that the diffusion of local electrons into the loss-cone caused by interaction with upper and lower band whistler chorus causes sufficient flux to explain the D-region electron density enhancements observed. However, there are other instances where better approximations are possible above 80 km or below 80 km but not simultaneously. This discrepancy indicates that the low-frequency whistler bands, responsible for scattering electrons with higher energy, and the high-frequency bands, responsible for lower energy precipitation, have a different duration and or different characteristic spatial scales.

Although UCLA-BERI-calculated density profiles undergo changes at various altitudes, the evolution of profiles calculated for VAP-A is replicated for VAP-B with better than 20% approximation in most altitudes and times and no more than 50% difference in the cases of largest difference at altitude above ~80 km. The close proximity of the in-situ wave and particle properties observed by both VAP spacecraft, which translates into similarity of $N_e$ profiles calculated from the precipitating electrons, show that the spacecraft are embedded in the same magnetospheric region and that the region has a spatial coherence of at least 1574 km, which is the in-situ separation between the two Van Allen Probes at 1550 UT. This distance is within the ~5000 km coherent scale size estimated for pulsating aurora (Nishimura et al., 2011) and approximately one order of magnitude smaller than the separation between either probe and the projection of PFISR into the magnetic equator using T96 magnetic field tracing. The corresponding inter-spacecraft separation in the ionosphere (130 km) is between two and three times smaller than the separation between PFISR's field-aligned beam and the foot-point of VAP-A (290 km) and VAP-B (390 km), respectively, with PFISR's location always north of either spacecraft's location. The distance between the radar's beam and either spacecraft foot-point is 3-4 times the size of the coherent scale size projected to the ionosphere.

The relatively large separation between either spacecraft and the projection of PFISR's flux tube is thus the likely reason for the lack of reasonable model-data agreement in the interval between 1529:42 UT and 1537:34 UT. Observed density is consistently lower than the predicted density in that interval. A plausible reason for the brief discrepancy during this time and quantitative approximation for the rest of the observation period is that, since PFISR's field-of-view is embedded in an ionospheric region northward of the foot-point of both Van Allen Probes, it likely maps to the tailward edge of the precipitation region where the Van Allen Probes are embedded or it maps to a different pulsating region. The instances of close model-data agreement indicate that, despite the spatial separation, PFISR may be measuring the effects of the whistler-electron interaction at the edge of the precipitation region that is being sampled by the Van Allen Probes. When the region's boundary moves earthward because of a temporal or spatial shift of the precipitation region, PFISR's flux tube migrates to the lower density region just outside. If PFISR is instead measuring the effects of an entirely separate region, then the close model-data approximation indicates that the wave properties at two adjacent pulsating regions are very similar.

**Acknowledgments.** This research was supported by NSF Collaborative Research Grant 1732365, and NSF AMISR Cooperative Agreement AGS-1840962. QM and JB are grateful for RBSP-ECT and EMFISIS funding provided by JHU/APL Contract 967399 and 921647 under NASA's Prime Contract NAS5- 01072. QM would like to acknowledge NASA grant 80NSSC20K0196. PFISR data are available through the AMISR data access repository https://amisr.com/amisr/links/data-access/. Van Allen Probes wave and particle data are available through the Van Allen Probes Science Gateway https://rbspgway.jhuapl.edu/. Results from the UCLA diffusion code are available at https://doi.org/10.6084/m9.figshare.16942696. Results from the BERI Monte Carlo simulations are available at 10.5281/zenodo.5651509.

## References


Abel, B., and R. M. Thorne (1998), Electron scattering loss in Earth's inner magnetosphere: 1. Dominant physical processes, J. Geophys. Res., 103(A2), 2385–2396, doi:10.1029/97JA02919.

Albert, J. M. (2003), Evaluation of quasi-linear diffusion coefficients for EMIC waves in a multispecies plasma, *J. Geophys. Res. (Space Physics)*, *108*, 1249, doi: 10.1029/ 2002JA009792.

Bilitza, D. (2001), International reference ionosphere 2000, Radio Science, 36(2), 261–275.

Blake, J.B., P.A. Carranza, S.G. Claudepierre, J.H. Clemmons, W.R. Crain, Y. Dotan, J.F. Fennell, F.H. Fuentes, R.M. Galvan, J.S. George, M.G. Henderson, M. Lalic, A.Y. Lin, M.D. Looper, D.J. Mabry, J.E. Mazur, B. McCarthy, C.Q. Nguyen, T.P. O'Brien, M.A. Perez, M.T. Redding, J.L. Roeder, D.J. Salvaggio, G.A. Sorensen, H.E. Spence, S. Yi, M.P. Zakrzewski, The magnetic electron ion spectrometer (MagEIS) instruments aboard the radiation belt storm probes (RBSP) spacecraft. Space Sci. Rev. (2013). doi:10.1007/s11214-013-9991-8

Bortnik, J., R. M. Thorne, N. P. Meredith, and O. Santolik (2007), Ray tracing of penetrating chorus and its implications for the radiation belts, *Geophys. Res. Lett.*, 34, L15109, doi:10.1029/2007GL030040.

Breneman, A. W., Crew, A., Sample, J., Klumpar, D., Johnson, A., Agapitov, O., Kletzing, C. A. (2017). Observations directly linking relativistic electron microbursts to whistler mode chorus: Van Allen Probes and FIREBIRD II. *Geophysical Research Letters, 44*, 11,265–11,272. https://doi.org/10.1002/2017GL075001

Clark, G., Tao, C., Mauk, B. H., Nichols, J., Saur, J., Bunce, E. J., et al. (2018). Precipitating electron energy flux and characteristic energies in Jupiter's main auroral region as measured by Juno/JEDI. Journal of Geophysical Research: Space Physics, 123, 7554–7567. https://doi.org/10.1029/2018JA025639.

Dougherty, J. P., and Farley, D. T. (1963), A theory of incoherent scattering of radio waves by a plasma: 3. Scattering in a partly ionized gas, *J. Geophys. Res.*, 68(19), 5473– 5486, doi:10.1029/JZ068i019p05473.

Funsten, H. O., Skoug, R. M., Guthrie, A. A., MacDonald, E. A., Baldonado, J. R., Harper, R. W., Chen, J. (2013). Helium, Oxygen, Proton, and Electron (HOPE) mass spectrometer for the Radiation Belt Storm Probes mission. Space Sci. Rev., 179, 423–484. https://doi.org/10.1007/s11214-013-9968-7.

Glukhov, V. S., V. P. Pasko, and U. S. Inan (1992), Relaxation of transient lower ionospheric dis- turbances caused by lightning-whistler-induced electron precipitation bursts, *J. Geophys. Res.*, *97*, 16,971–16979, doi: 10.1029/92JA01596.

Heinselman, C. J., and M. J. Nicolls (2008), A Bayesian approach to electric field and E-region neutral wind estimation with the Poker Flat Advanced Modular Incoherent Scatter Radar, *Radio Sci., 43*, RS5013, doi:10.1029/2007RS003805.

Horne, R. B., and R. M. Thorne (2003), Relativistic electron acceleration and precipitation during resonant interactions with whistler-mode chorus, *Geophys. Res. Lett.*, *30*, 1527, doi:10.1029/2003GL016973.

Kasahara, S. et al. (2018), Pulsating aurora from electron scattering by chorus waves, *Nature*, *554*, 338, doi:10.1038/nature25505

Kennel, C. F. (1969), Consequences of a magnetospheric plasma, *Rev. Geophys., 7*, 379–419.

Kennel, C. F., and H. E. Petschek (1966), Limit on stably trapped particle fluxes, *J. Geophys. Res.*, *71*, 1.

Kletzing, C. A., et al. (2013), The Electric and Magnetic Field Instrument Suite with Integrated Science (EMFISIS) on the RBSP, Space Sci. Rev., 179, 127– 181, doi:10.1007/s11214-013-9993-6.

Kurth, W. S., De Pascuale, S., Faden, J. B., Kletzing, C. A., Hospodarsky, G. B., Thaller, S. and Wygant, J. R. (2015), Electron densities inferred from plasma wave spectra obtained by the Waves instrument on Van Allen Probes. J. Geophys. Res. Space Physics, 120, 904–914. doi: 10.1002/2014JA020857.

Lehtinen, N. G., T. F. Bell, and U. S. Inan (1999), Monte Carlo simulation of runaway MeV electron breakdown with application to red sprites and terrestrial gamma ray flashes, Journal of Geophysical Research, 104(A11), 24699–24712.

Lehtinen, N. G. (2000), Relativistic runaway electrons above thunderstorms, Ph.D. thesis, Stanford University.

Lehtinen, N. G., and U. S. Inan (2007), Possible persistent ionization caused by giant blue jets, *Geophys. Res. Lett.*, *34*, L08804, doi: 10.1029/2006GL029051.

Liang, J., B. Ni, E. Spanswick, M. Kubyshkina, E. F. Donovan, V. M. Uritsky, R. M. Thorne, and V. Angelopoulos (2011), Fast earthward flows, electron cyclotron harmonic waves, and diffuse auroras: Conjunctive observations and a synthesized scenario, *J. Geophys. Res., 116*, A12220, doi:10.1029/2011JA017094.

Lorentzen, K. R., J. B. Blake, U. S. Inan, and J. Bortnik (2001), Observations of relativistic electron microbursts in association with VLF chorus, *J. Geophys. Res.*, *106*, 6017–6027, doi: 10.1029/2000JA003018.

Ma, Q., H. K. Connor, X.-J. Zhang, W. Li, X.-C. Shen, D. Gillespie, et al. (2020), Global survey of plasma sheet electron precipitation due to whistler mode chorus waves in Earth's magnetosphere, Geophysical Research Letters, 47, e2020GL088798, doi:10.1029/2020GL088798.

Ma, Q., Li, W., Zhang, X.-J., Bortnik, J., Shen, X.-C., Connor, H. K., et al. (2021). Global survey of electron precipitation due to hiss waves in the Earth’s plasmasphere and plumes. Journal of Geophysical Research: Space Physics, 126, e2021JA029644. https://doi.org/10.1029/2021JA029644.

Marshall, R. A., M. Nicolls, E. Sanchez, N. G. Lehtinen, and J. Neilson (2014), Diagnostics of an artificial relativistic electron beam interacting with the atmosphere, *Journal of Geophysical Research (Space Physics)*, *119*, 8560–8577, doi: 10.1002/2014JA020427.

Marshall, R. A., W. Xu, A. Kero, R. Kabirzadeh, and E. Sanchez (2019), Atmospheric effects of a relativistic electron beam injected from above: Chemistry, electrodynamics, and radio scattering, Frontiers in Astronomy and Space Sciences, 6, 6.

Mathews, J. D. (1978), The effects of negative ions on collision-dominated Thomson scattering, *J. Geophys. Res., 83*, 505–512.

Mauk, B. H., N. J. Fox, S. G. Kanekal, R. L. Kessel, D. G. Sibeck, and A. Ukhorskiy (2013), Science objectives and rationale for the radiation belt storm probes mission, *Space Sci. Rev.*,179, 3–27, doi:10.1007/s11214-012-9908-y.

Millan, R. M., and R.M. Thorne, Review of radiation belt relativistic electron losses, (2007), J. Atmos Solar-Terrestrial Phys., 69, 362, doi:10.1016/j.jastp.2006.06.019

Millan, R. M., M. P. McCarthy, J. G. Sample, D. M. Smith, L. D. Thompson, D. G. McGaw, L. A. Woodger, J. G. Hewitt, M. D. Comess, K. B. Yando, A. X. Liang, B. A. Anderson, N. R. Knezek, W. Z. Rexroad, J. M. Scheiman, G. S. Bowers, A. J. Halford, A. B. Collier, M. A. Clilverd, R. P. Lin, and M. K. Hudson, (2013), The balloon array for Van Allen Probes relativistic electron losses (BARREL), *Space Sci. Rev.*, *179*, 503–530, doi: 10.1007/s11214-013-9971-z.

Miyoshi, Y., et al. (2015), Energetic electron precipitation associated with pulsating aurora: EISCAT and Van Allen Probe observations, *J. Geophys. Res. Space Physics*, 120, 2754–2766, doi:10.1002/2014JA020690.

Mozer, F. S., Agapitov, O. V., Blake, J. B., & Vasko, I. Y. (2018). Simultaneous observations of lower band chorus emissions at the equator and microburst precipitating electrons in the ionosphere. *Geophysical Research Letters*, 45, 511– 516. https://doi.org/10.1002/2017GL076120

Ni, B., J. Bortnik, Y. Nishimura, R. M. Thorne, W. Li, V. Angelopoulos, Y. Ebihara, and A. T. Weatherwax (2014), Chorus wave scattering responsible for the Earth's dayside diffuse auroral precipitation: A detailed case study, *J. Geophys. Res. (Space Physics)*, 119, 897–908, doi:10.1002/2013JA019507.

Ni, B., R. M. Thorne, Y. Y. Shprits, and J. Bortnik (2008), Resonant scattering of plasma sheet electrons by whistler-mode chorus: Contribution to diffuse auroral precipitation, *Geophys. Res. Lett.*, *35*, L11106, doi:10.1029/2008GL034032.

Ni, B., R. M. Thorne, N. P. Meredith, R. B. Horne, and Y. Y. Shprits (2011), Resonant scattering of plasma sheet electrons leading to diffuse auroral precipitation: 2. Evaluation for whistler mode chorus waves, *J. Geophys. Res. (Space Physics)*, *116*, A04219, doi: 10. 1029/2010JA016233.

Ni, B., J. Liang, R. M. Thorne, V. Angelopoulos, R. B. Horne, M. Kubyshkina, E. Spanswick, E. F. Donovan, and D. Lummerzheim (2012), Efficient diffuse auroral electron scattering by electro- static electron cyclotron harmonic waves in the outer magnetosphere: A detailed case study, *J. Geophys. Res. (Space Physics)*, *117*, A01218, doi: 10.1029/2011JA017095.

Nicolls, M. J., C. J. Heinselman, E. A. Hope, S. Ranjan, M. C. Kelley, and J. D. Kelly (2007), Imaging of Polar mesosphere summer echoes with the 450-MHz Poker Flat Advanced Modular Incoherent Scatter Radar, *Geophys. Res. Lett., 34*, L20102, doi:10.1029/2007GL031476.

Nicolls, M. J., R. H. Varney, S. L. Vadas, P. A. Stamus, C. J. Heinselman, R. B. Cosgrove, and M. C. Kelley (2010), Influence of an inertia-gravity wave on mesospheric dynamics: A case study with the Poker Flat Incoherent Scatter Radar, *J. Geophys. Res., 115*, D00N02, doi:10.1029/2010JD014042.

Nishimura, Y. et al. Identifying the driver of pulsating aurora. Science 330, 81–84 (2010).

Nishimura, Y., et al. (2011), Multievent study of the correlation between pulsating aurora and whistler mode chorus emissions, J. Geophys. Res., 116, A11221, doi:10.1029/2011JA016876.

Ozaki, M., Miyoshi, Y., Shiokawa, K. *et al.* Visualization of rapid electron precipitation via chorus element wave–particle interactions. *Nat Commun* **10,** 257 (2019). https://doi.org/10.1038/s41467-018-07996-z

Picone, J. M., Hedin, A. E., Drob, D. P., and Aikin, A. C., NRLMSISE-00 empirical model of the atmosphere: Statistical comparisons and scientific issues, *J. Geophys. Res.*, 107( A12), 1468, doi:10.1029/2002JA009430, 2002.

Rosenberg, T. J., Helliwell, R. A., & Katsufrakis, J. P. (1971). Electron precipitation associated with discrete very-low-frequency emissions. *Journal of Geophysical Research, 76(34)*, 8445–8452. https://doi.org/10.1029/JA076i034p08445

Ross, J. P. J., Glauert, S. A., Horne, R. B., Watt, C. E., Meredith, N. P., & Woodfield, E. E. (2020). A new approach to constructing models of electron diffusion by EMIC waves in the radiation belts. Geophysical Research Letters, 47, e2020GL088976. https://doi.org/10.1029/2020GL088976

Spence, H. E., et al. (2013), Science goals and overview of the Radiation Belt Storm Probes (RBSP) Energetic Particle, Composition, and Thermal Plasma (ECT) suite on NASA's Van Allen Probes mission, Space Sci. Rev., 179(1-4), 311–336, doi:10.1007/s11214-013-0007-5.

Summers, D., and R. M. Thorne (2003), Relativistic electron pitch-angle scattering by electromagnetic ion cyclotron waves during geomagnetic storms, *J. Geophys. Res. (Space Physics)*, *108*, 1143, doi: 10.1029/2002JA009489.

Thorne, R. M. (2010), Radiation belt dynamics: The importance of wave-particle interactions, *Geophys. Res. Lett.*, 37, L22107, doi:10.1029/2010GL044990.

Thorne, R. M., B. Ni, X. Tao, R. B. Horne, and N. P. Meredith (2010), Scattering by chorus waves as the dominant cause of diffuse auroral precipitation, Nature, 467, 943{946, doi:10.1038/nature09467.

Thorne, R. M., E. J. Smith, R. K. Burton, and R. E. Holzer (1973), Plasmaspheric hiss, *J. Geophys. Res.*, *78*, 1581–1596, doi: 10.1029/JA078i010p01581.

Tsyganenko N. A., A Magnetospheric magnetic field model with a warped tail current sheet, Planet. Space Sci., 37, 5-20, DOI: 10.1016/0032-0633(89)90066-4, 1989.

Tsyganenko N. A., Effects of the solar wind conditions on the global magnetospheric configuration as deduced from data-based field models, in European Space Agency Publication ESA SP-389, p.181, 1996.

Tsyganenko N. A., A model of the near magnetosphere with a dawn-dusk asymmetry - 2. Parameterization and fitting to observations, J. Geophys.Res., 107, A7, DOI: 10.1029/2001JA000220, 2002.

Turunen, E., P. T. Verronen, A. Seppälä, C. J. Rodger, M. A. Clilverd, J. Tamminen, C.-F. Enell, and T. Ulich (2009), Impact of different energies of precipitating particles on NO*x* generation in the middle and upper atmosphere during geomagnetic storms, *J. Atmospheric and Solar-Terrestrial Physics*, *71*, 1176–1189, doi: 10.1016/j.jastp.2008.07.005.

Xu, W., R. A. Marshall, H. N. Tyssøy, and X. Fang (2020), A Generalized Method for Calculating Atmospheric Ionization by Energetic Electron Precipitation, Journal of Geo-physical Research: Space Physics, 125(11), e2020JA028482.

Xu, W., Marshall, R. A., Fang, X., Turunen, E., & Kero, A. (2018). On the effects of bremsstrahlung radiation during energetic electron precipitation. Geophysical Research Letters, 45, 1167–1176.

Zhang, X.-J., et al. (2016), Direct evidence for EMIC wave scattering of relativistic electrons in space, J. Geophys. Res. Space Physics, 121, 6620– 6631, doi:10.1002/2016JA022521.